Multidimensional coupling owing to optical nonlinearities. II. Results

Robert E. Bridges,* Robert W. Boyd, and Govind P. Agrawal

The Institute of Optics, University of Rochester, Rochester, New York 14627

Received January 23, 1995; revised manuscript received August 15, 1995

We compare three computational techniques developed in the preceding paper [J. Opt. Soc. Am. **13,** 553 (1996)] that account for the effects of nonlinear coupling on light propagating through nonlinear, dispersive media. We demonstrate that all three techniques give reasonable accuracy under conditions typical of a self-mode-locked laser. We further show that these techniques are greatly superior to techniques that neglect nonlinear coupling in that they give results that are more accurate and, in some cases, qualitatively different. We demonstrate such a qualitative difference by using the example of a self-mode-locked (Kerr-lens mode-locked) Ti:sapphire laser that has only one cavity solution when nonlinear coupling is included yet two cavity solutions when nonlinear coupling is neglected. © 1996 Optical Society of America

1. INTRODUCTION

The preceding paper[1] (Paper I) describes three techniques for calculating the behavior of a beam propagating in a nonlinear, dispersive medium. The most accurate of these uses the beam-propagation method (BPM) with three-dimensional fast Fourier transforms (3D FFT's) to solve the generalized propagation equation (I.8).[1] A faster technique uses the BPM with one-dimensional (1D) FFT's to solve three coupled differential equations, Eqs. (I.16). The fastest but least accurate technique uses six coupled equations based on second moments (second-moment equations, SME's), Eqs. (I.28) or (I.29).

In this paper we demonstrate that all three techniques give comparable results when applied to a self-mode-locked laser under the influence of diffraction, second-order dispersion, and Kerr nonlinearity. We show that all three techniques are greatly superior to techniques that neglect nonlinear coupling in that they give results that are more accurate and, in some cases, qualitatively different.

The remainder of this paper leads in stages to an analysis of the self-mode-locked (Ti:sapphire) laser. We begin by considering the propagation effects in such a laser, first for the simplest (quasi-cw) case in which dispersion is neglected and then for the more complex (short-pulse) case in which dispersion is included. We account for propagation through optical elements such as mirrors, angled interfaces, and prism pairs. Finally, we obtain a self-consistent description of the laser behavior by including the effects of the cavity itself.

2. PROPAGATION IN A NONLINEAR MEDIUM

A beam of the sort found in a cw Ti:sapphire laser might have an intracavity power of a few watts or a few tens of watts, which is too small to produce any significant effects because of the Kerr nonlinearity. The beam in a self-mode-locked laser, however, has an intracavity power that is several orders of magnitude larger, making the Kerr nonlinearity important.

In this section and the next, we consider the propagation of light in a Kerr medium. We first discuss the quasi-cw case in which there is a negligible change in pulse width owing to dispersion. This approximation is very good for pulse widths greater than 1 ps and fairly good for pulses as short as 100 fs. With this approximation the temporal evolution is not relevant, and we can use Eqs. (I.17) or (I.30). In Section 3 we discuss the short-pulse case in which dispersion effects need to be included.

We consider for definiteness the example of a beam propagating through a Ti:sapphire crystal. This material has a positive coefficient of nonlinearity, n_2, which means that it also has a positive critical power, P_c, because $P_c = 2\pi n_0/\beta_0^2 n_2$. We assume that the beam has a Gaussian profile and that it reaches its beam waists (in both x and y) as it enters the Ti:sapphire crystal at position $z = 0$. We assume that the beam has initial rms widths of $\rho_x = 12\ \mu$m and $\rho_y = 6\ \mu$m (corresponding to the conventionally used w widths[2] of $w_x = 24\ \mu$m and $w_y = 12\ \mu$m).

The curves of Fig. 1 show the evolution of ρ_x and ρ_y as a function of the propagation distance z. The dashed curves show the evolution for a negligible Kerr nonlinearity ($P \ll P_c$). We obtain these curves by using the second-moment equation (I.30a) with $P = 0$. The solid curves show the evolution for a Kerr nonlinearity typical of a self-mode-locked laser ($P = P_c/2$). We obtain the solid curves labeled 1 from Eqs. (I.30a) by making the (invalid) assumption that the nonlinear coupling effects can be neglected. The ellipticity factors are (artificially) set equal to one ($\epsilon_x^{(2)} = 1$ and $\epsilon_y^{(2)} = 1$) to remove the nonlinear coupling from the calculations. (Recall from Paper I that the two-dimensional ellipticity factors are defined as $\epsilon_x^{(2)} = \rho_x/\rho_y$ and $\epsilon_y^{(2)} = \rho_y/\rho_x$.) We see that the physical effect of the Kerr nonlinearity is to reduce the beam widths, ρ_x and ρ_y.

We obtain the solid curves labeled 2 by using the coupled SME's. These curves include the effects of nonlinear coupling and hence are more accurate than the curves

0740-3224/96/030560-10$06.00

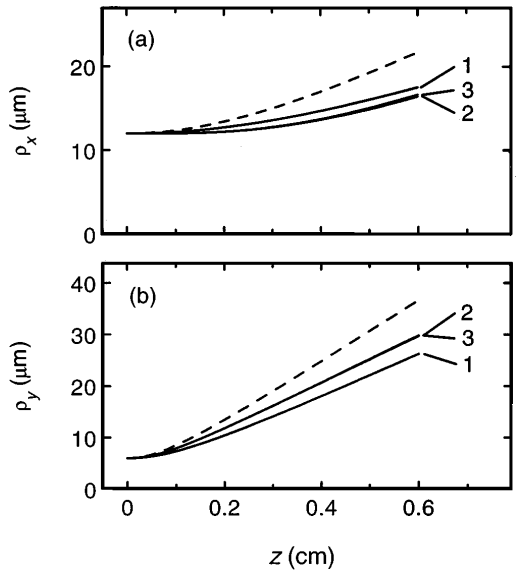

Fig. 1. Rms width ρ_x or ρ_y of an elliptical beam propagating in Ti:sapphire under quasi-cw conditions. Dashed curves account for linear effects only; solid curves account not only for linear effects but also for Kerr nonlinearity. The three solid curves in each figure are found as follows: 1, neglecting nonlinear coupling; 2, using SME's; and 3, applying the BPM with 1D FFT's to coupled differential equations.

labeled 1. We obtain them by dividing the medium into small steps and then using Eqs. (I.30) to calculate ρ_x^2, ρ_y^2, R_x, and R_y at each step. The ellipticity factors, $\epsilon_x^{(2)}$ and $\epsilon_y^{(2)}$, are also calculated at each step to provide the nonlinear coupling. We see that the physical effect of nonlinear coupling is to change ρ_x and ρ_y. We can understand the nature of this change by noting that $\rho_x > \rho_y$ in the vicinity of the beam waist, from which it follows that $\epsilon_x^{(2)} > \epsilon_y^{(2)}$. The nonlinear term in Eq. (I.30a) is then larger in x than in y. Consequently, in the vicinity of the beam waist, ρ_x shrinks more when nonlinear coupling is included, and ρ_y shrinks less. The curves labeled 1 and 2 differ by as much as 11%, indicating the importance of the nonlinear coupling. We will see below that this difference is even more significant inside a laser cavity.

We obtain the solid curves labeled 3 by using the BPM with 1D FFT's to solve the coupled differential equations (I.17). After each step the effective widths, $\delta_x = (\int_{-\infty}^{\infty} |u_x|^4 \mathrm{d}x)^{-1}$ and $\delta_y = (\int_{-\infty}^{\infty} |u_y|^4 \mathrm{d}y)^{-1}$, are calculated to provide the nonlinear coupling. The curves labeled 3 are more accurate than those labeled 2; however, curves 2 and 3 are similar: they differ by less than 1.3% at all points.

The differences in curves 2 and 3 are the result of changes in the beam profiles that occur during propagation. To demonstrate that this is the case, we first use the BPM to calculate the beam-quality factors, σ_x and σ_y, as shown in Fig. 2(a), and the nonlinear shape factors, η_x and η_y, as shown in Fig. 2(b). Using these values for σ_x, σ_y, η_x, and η_y, we find that the second-moment equations (I.30) give the same results (to within 0.01%) as the BPM when used with 1D FFT's to solve Eqs. (I.17).

We can further improve the accuracy of the calculations by using the BPM with two-dimensional (2D) FFT's, as described in Sec. 3 of Paper I. This technique requires more computation time than the BPM with 1D FFT's, as indicated in Appendix A, but is accurate even if the separability assumption, Eq. (I.12), does not hold. The curves that we obtain by using 2D FFT's are the same (to within 0.1%) as the curves labeled 3 in Fig. 1. This demonstrates that the separability assumption is a good one in this case.

One may wonder why the 1D FFT calculation is so accurate. To understand better the origin of the error in the 1D FFT calculations, we plot in Fig. 3 the quantity $\Delta = |I_{xy}/I_{xy0} - I_x I_y / I_{x0} I_{y0}|$ throughout the $x-y$ plane. Here $I_{xy}(x, y)$ is the intensity calculated with 2D FFT's and $I_x(x)$ and $I_y(y)$ are the intensities calculated with 1D FFT's. The subscript 0 indicates the intensity at the center of the beam. We see that Δ is zero (to within one part in 10^8) along the x and y axes and rises to nearly 2% off-axis. This indicates that, although the field amplitudes are not precisely separable, they are nearly separable over most of the beam, especially near the axes, where the intensity is highest. The net effect is to produce a very small difference in the results obtained with 1D and 2D FFT's.

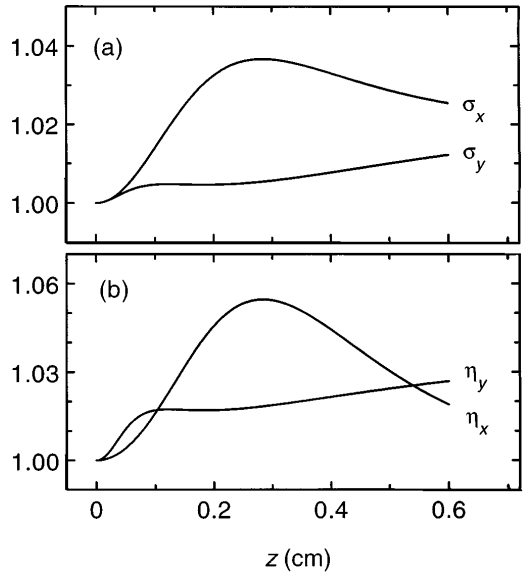

Fig. 2. Evolution of (a) beam-quality factors σ_x and σ_y and (b) nonlinear shape factors η_x and η_y.

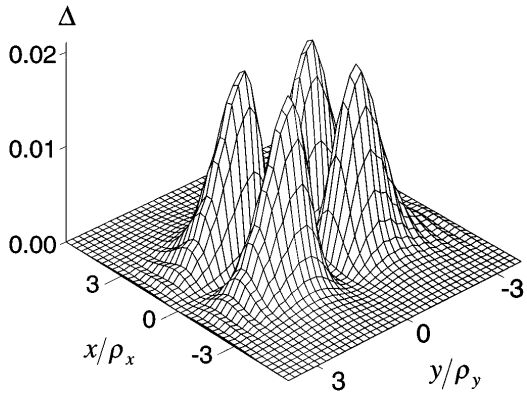

Fig. 3. Transverse variation in the relative error $\Delta = |I_{xy}/I_{xy0} - I_x I_y / I_{x0} I_{y0}|$. Here $I_{xy}(x, y)$ is the intensity calculated with 2D FFT's and $I_x(x)$ and $I_y(y)$ are the intensities calculated with 1D FFT's. The subscript 0 in this expression indicates the intensity at the center of the beam.

The main conclusion that we draw from this section is that accuracy depends on the computational method used. With nonlinear coupling included, the computational errors in this example were found to be relatively small: less than 0.1% for the BPM with 1D FFT's and less than 1.3% for the SME's. With nonlinear coupling neglected, however, the errors were found to be much larger: as large as 11%. Later in this paper, we will see that these differences in accuracy have important implications for self-mode-locked lasers.

3. PROPAGATION IN A NONLINEAR, DISPERSIVE MEDIUM

To understand the evolution of a pulse propagating in a nonlinear, dispersive medium, we use the definition $z_{dt} = -2\rho_t^2/\beta_2$, along with Eqs. (I.21), (I.22), and (I.28b), to obtain

$$\frac{\partial \rho_t^2(z_1 + h)}{\partial z} = \beta_2 C_{t1} + \frac{\beta_2^2 h}{2\rho_{t1}^2}\left(\sigma_t^2 + C_{t1}^2\right) + \frac{\beta_2 h}{2\rho_{t1}^2}\,\frac{\epsilon_t^{(3)}\eta_{xyt}}{\beta_0}\,\frac{U}{P_c}. \tag{1}$$

Consider the three terms on the right-hand side of Eq. (1). The first term shows that, initially, the second-order dispersion may cause either an increase or a decrease in the pulse width, depending on the signs of C_{t1} and β_2. The second term shows that, eventually (after the pulse propagates far enough), the second-order dispersion produces a monotonic increase in pulse width. The third term shows that the Kerr nonlinearity may produce either an increase or a decrease in pulse width, depending on the signs of β_2 and P_c. In Ti:sapphire at $\lambda_0 = 800$ nm,[3] both β_2 and P_c are positive, leading to an increase in ρ_t during propagation.

In this section we consider the example of a beam propagating through 6 mm of Ti:sapphire at a wavelength of 800 nm. We assume that the electric field amplitude has a profile in time that is initially a hyperbolic secant with an rms width of 15 fs, corresponding to a FWHM of 29.2 fs. We assume that the beam has a Gaussian profile in x and y and that it reaches its beam waists (in x, y, and t) as it enters the Ti:sapphire material at the position $z = 0$. We take the initial rms widths to be $\rho_x = 12$ μm and $\rho_y = 6$ μm.

We ignore the third-order dispersion in this example because it produces a change in the pulse width of less than 0.02% under these conditions.[4] (The third-order dispersion also causes a slight asymmetry in the pulse by shifting the mean value to $\langle t \rangle \approx 10^{-3}\rho_t$.)

As shown in Eqs. (I.28), the pulse energy U determines the strength of the Kerr nonlinearity. However, for ease of comparison with the 2D case, we here define the reference power as $P_r = U/\delta_{t0}$, where $\delta_{t0} = 2\sqrt{\pi}\rho_{t0}/\eta_{t0}$ and ρ_{t0} is the rms pulse width at $z = 0$. [To understand the motivation for defining the reference power in this way, note the definition for the effective power given in the text preceding Eqs. (I.30).]

The curves of Fig. 4 show the evolution of ρ_x, ρ_y, and ρ_t as a function of propagation distance z. The dashed curves show the evolution for a negligible Kerr nonlinearity ($U \ll P_c\delta_{t0}$). We obtain these curves by using the second-moment equation (I.28a) with $U = 0$. The solid curves of Fig. 4 show the evolution of the beam for a Kerr nonlinearity typical of a self-mode-locked laser ($P_r = P_c/2$). We obtain the solid curves labeled 1 from Eq. (I.28a) by making the (invalid) assumption that nonlinear coupling effects can be neglected. The ellipticity factors are artificially set to $\epsilon_x^{(3)} = \epsilon_y^{(3)} = 1/2\sqrt{\pi}\rho_{t0}$ and $\epsilon_t^{(3)} = \rho_t/2\sqrt{\pi}\rho_{x0}\rho_{y0}$ to remove nonlinear coupling from the calculations. Here, ρ_{x0} and ρ_{y0} are the rms widths at $z = 0$. (Recall from Paper I that the three-dimensional ellipticity factors are defined as $\epsilon_\nu^{(3)} = \rho_\nu^2/2\sqrt{\pi}\rho_x\rho_y\rho_t$.) We see that the physical effect of the Kerr nonlinearity when n_2 and β_2 are positive is to decrease the beam widths ρ_x and ρ_y and to increase the pulse width ρ_t.

The solid curves labeled 2 are obtained by use of the coupled SME's. These curves include the effects of nonlinear coupling and hence are more accurate than the curves labeled 1. We obtain them by dividing the medium into small steps and then using Eqs. (I.28) to calculate ρ_x^2, ρ_y^2, ρ_t^2, C_x, C_y, and C_t at each step. The ellipticity factors, $\epsilon_x^{(3)}$, $\epsilon_y^{(3)}$, and $\epsilon_t^{(3)}$, are also calculated at each step to provide the nonlinear coupling. We see that the physical effect of nonlinear coupling in this case is to decrease ρ_x and ρ_t and increase ρ_y. The curves labeled 1 and 2 differ by as much as 15%, indicating the importance of the nonlinear coupling.

We obtain the solid curves labeled 3 by using the BPM with 1D FFT's to solve the coupled differential equations (I.16). After each step the effective widths, δ_x, δ_y, and δ_t, are calculated to provide the nonlinear coupling. The curves labeled 3 are more accurate than

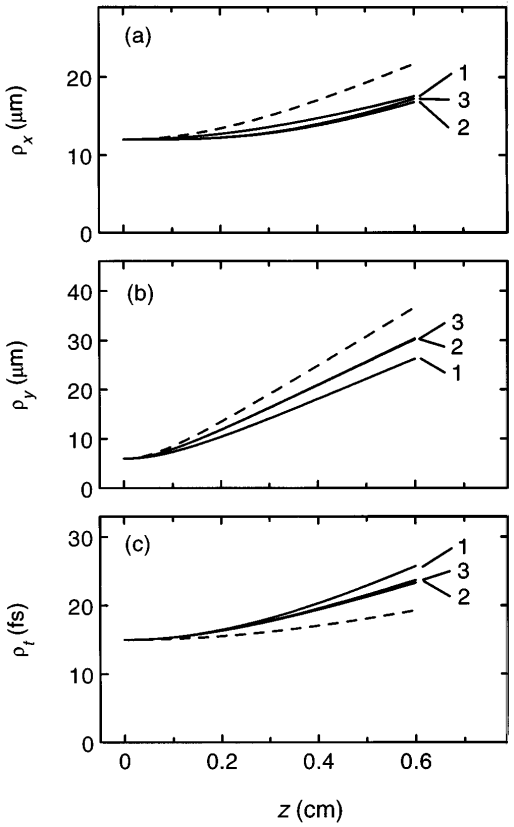

Fig. 4. Same as Fig. 1 but for the three widths ρ_x, ρ_y, and ρ_t and for an input pulse width of 15 fs.

those labeled 2; however, curves 2 and 3 are similar: they differ by less than 2.5% at all points.

The differences in the curves labeled 2 and 3 are the results of changes in the beam profiles that occur during propagation. To demonstrate that this is the case, we first use the BPM to calculate the beam-quality factors, σ_x and σ_y, and the nonlinear shape factors, η_x and η_y. Using these values for σ_x, σ_y, η_x, and η_y, we find the same results (to within 0.05%) in using the second-moment equations (I.28) as in using the BPM with 1D FFT's to solve Eqs. (I.16).

The main conclusion of this section is that there are important nonlinear coupling effects among all three spatiotemporal (x, y, t) dimensions that can be accounted for by the techniques developed in Paper I. For the example considered in this section the errors were found to be relatively small when the techniques of Paper I were used but much larger when nonlinear coupling was ignored.

4. PROPAGATION THROUGH OPTICAL ELEMENTS

Thus far we have considered the propagation of a beam through a homogeneous medium. We now want to include optical elements used in constructing laser cavities, for example, mirrors, lenses, angled interfaces, prisms, and apertures.

It is possible to recast the second-moment equations (I.28)–(I.30) as *ABCD* matrices.[5,6] This approach permits the easy integration of optical elements whose actions on the beam can also be treated through the appropriate *ABCD* matrices.[7] However, this approach becomes cumbersome when additional physical effects, such as thermal lensing and saturated gain, are considered. Furthermore, *ABCD* methods are applicable only to SME's and not to the coupled differential equations (I.16)–(I.18) that are solved by the BPM.

In this section we develop a general method for including the effects of optical elements. We begin by decomposing each optical element into its parts. A lens, for example, is composed of two surfaces and an intervening propagation distance. We treat the intervening propagation distance by using the techniques discussed in Sections 2 and 3. Some other elements, such as mirrors and angled interfaces, consist of a single surface. Prism pairs and apertures are somewhat more complicated and will be treated presently.

The surfaces of the optical elements affect the electric field amplitudes only in the x and y directions (not in the t direction). In other words (following the notation of Section 3 of Paper I), the surfaces affect u_x and u_y but not u_t. We make the usual assumptions that the surfaces have zero thickness and that they perform just two transformations on u_x and u_y: (1) multiplication by a quadratic phase factor and (2) rescaling to change the width, ρ_x or ρ_y. The effect of these approximations is to neglect the geometrical aberrations[8] such as spherical aberration[9] and coma.[10]

Under these assumptions an easy way to determine the transformation operations of the surfaces of the optical elements is by using *ABCD* matrices, which are well known for a variety of optical elements.[7] We now derive formulas that extract from these *ABCD* matrices the information that one needs to perform the transformations.

We designate the elements of the *ABCD* matrix in the ν dimension as

$$M_\nu = \begin{bmatrix} \tilde{A}_\nu & \tilde{B}_\nu \\ \tilde{C}_\nu & \tilde{D}_\nu \end{bmatrix}, \tag{2}$$

where $\nu = x$ or $\nu = y$. The tildes have been placed over the elements to prevent confusion between the matrix element $\tilde{C}_\nu$ and the chirp parameter C_ν.

The matrix element $\tilde{B}_\nu$ is given by $\tilde{B}_\nu = h/n_0$, where h is the propagation distance. For a single surface, this element vanishes because $h = 0$. We use the reduced q parameter,[11] defined by the relation

$$\frac{1}{q_\nu} = \frac{n_0}{R_\nu} + i\frac{\lambda_0}{4\pi\rho_\nu^2}, \tag{3}$$

along with the transformation rule for real *ABCD* matrix elements,[11] which for $\tilde{B}_\nu = 0$ can be written as

$$\frac{1}{q_{\nu 2}} = \frac{\tilde{C}_\nu}{\tilde{A}_\nu} + \frac{\tilde{D}_\nu}{\tilde{A}_\nu}\,\frac{1}{q_{\nu 1}}. \tag{4}$$

Here the subscripts 1 and 2 represent the positions just before and after the interface, respectively. Substituting Eq. (3) into Eq. (4) and separating the real and imaginary parts, we obtain two equations:

$$\frac{n_{02}}{R_{\nu 2}} = \frac{\tilde{C}_\nu}{\tilde{A}_\nu} + \frac{\tilde{D}_\nu}{\tilde{A}_\nu}\,\frac{n_{01}}{R_{\nu 1}}, \tag{5}$$

$$\rho_{\nu 2} = \rho_{\nu 1}\sqrt{\tilde{A}_\nu/\tilde{D}_\nu}. \tag{6}$$

Equation (6) gives the change in width in the dimension ν.

To determine the change in phase we use the relation for chirp parameter C_ν given in Sec. 4 of Paper I, $C_\nu = -z_{d\nu}/R_\nu = -4\pi n_0\rho_\nu^2/\lambda_0 R_\nu$. We use this relation, which is valid for $\nu = x$ or $\nu = y$, to substitute for $n_{01}/R_{\nu 1}$ and $n_{02}/R_{\nu 2}$ in Eq. (5), and we use Eq. (6) to substitute for $\tilde{D}_\nu$ in Eq. (5). The result is

$$C_{\nu 2} = C_{\nu 1} - \frac{4\pi\rho_{\nu 1}^2}{\lambda_0}\,\frac{\tilde{C}_\nu}{\tilde{D}_\nu}. \tag{7}$$

Following Eq. (I.24), we obtain

$$u_{\nu 2}(\nu; z) = u_{\nu 1}(\nu; z)\exp\left(i\,\frac{\pi}{\lambda_0}\,\frac{\tilde{C}_\nu}{\tilde{D}_\nu}\,\nu^2\right). \tag{8}$$

When using the BPM, we use Eqs. (6) and (8) to account for the action of optical elements; when using the SME's, we use Eqs. (6) and (7).

The most important optical element for controlling the temporal behavior of the pulse is the prism pair. It can be shown that a prism pair is equivalent to two elements, an identical prism pair with zero intraprism path length and a block of prism material of thickness equal to the intraprism path length.[12,13] The second-order dispersion parameter for the prism pair of zero intraprism path length is to a good approximation[13]

$$\beta_2 = -\frac{2\lambda_0^3}{\pi c^2}\left(\frac{\mathrm{d}n}{\mathrm{d}\lambda}\right)_{\lambda_0}^2, \tag{9}$$

where n is the index of refraction of the prism material and λ_0 is the wavelength of the center of the spectrum. For short pulses, it may also be necessary to consider the third- and fourth-order dispersive effects of the prism pair.[14]

Self-mode locking may be obtained through the use of either a hard aperture or a soft aperture. To model the action of a soft aperture it is necessary to account for the effects of saturated gain, and that is beyond the scope of this paper. The action of a hard aperture needs to be modeled only when the beam shape is changed significantly by diffraction from the edges of the aperture. Whether the change in beam shape is significant will depend on the specific laser being considered, but it is known that truncating even a small fraction of a beam can produce relatively large ripples in the diffraction pattern.[15] In performing calculations the presence of a hard aperture will usually increase the computation time, even if an optimized numerical method (such as the continuous Fourier transform[16]) is used. It has been suggested that hard apertures can produce many effects, including self-starting of mode locking[17] and unidirectional operation in self-mode-locked ring lasers.[18]

5. CAVITY SOLUTIONS

The effects of nonlinear coupling are often made more dramatic by the presence of a cavity. In some cases calculations that include nonlinear coupling lead to results that differ qualitatively from those obtained when nonlinear coupling is neglected. We now consider the example of a specific cavity that exhibits such qualitative differences.

A type of cavity that is often used for the self-mode-locked Ti:sapphire laser is the Z-shaped cavity shown in Fig. 5(a). Near the center of this cavity is a Ti:sapphire crystal, which provides both the gain and the Kerr nonlinearity for the laser. On either side of this is a curved folding mirror that focuses light into the crystal. At the ends of the cavity are flat end mirrors, one of which is the output coupler, labeled OC. A prism pair is placed in the cavity to provide dispersion compensation.

For short pulses it is necessary to account for the dispersive properties of both the prism pair and the Ti:sapphire crystal. In this section we consider the somewhat simpler quasi-cw case of a pulse that is relatively long (say, 100 fs). The width ρ_t of such a pulse does not change appreciably during propagation, which allows us to use Eqs. (I.30) by defining the effective power as $P = U/\delta_t = U\eta_t/2\sqrt{\pi}\rho_t$. We can replace the cavity of Fig. 5(a) with the equivalent cavity of Fig. 5(b) because we no longer need to consider explicitly the prism pair. The distances of Fig. 5(b) are $L_1 = L_2 = 80$ cm, $d_1 = 4.85$ cm, $d_2 = 4.95$ cm, $t = 1.5$ cm, and $R_1 = R_2 = 10$ cm. The angles are $\theta_1 = \theta_2 = 27°$.

We now proceed to find the cavity solutions for three cases: the cw case, the mode-locked case with nonlinear coupling neglected, and the mode-locked case with nonlinear coupling included. For the cw case we easily find the fundamental cavity solution shown in Fig. 6 by using the *ABCD* matrix technique.[19] The horizontal axes of these figures give the position z within the cavity, with $z = 0$ at the center of the crystal and $z < 0$ on the side of the output coupler. The vertical axis indicates the rms width ρ_ν. For definiteness, we use the subscripts $\nu = x$ and $\nu = y$ to designate the tangential and the sagittal planes, respectively. Figure 6(a) shows the entire cavity, and Fig. 6(b) shows a magnified view in the vicinity of the crystal. Because we are neglecting transverse variations in the cavity that result from gain or loss, and because the end mirrors are flat, the beam in Fig. 6(a) comes to a waist in the x and the y directions at the end mirrors.[19,20] The beam in Fig. 6(b) undergoes a discontinuous change in width in the tangential (x) direction, indicating the edges of the crystal.

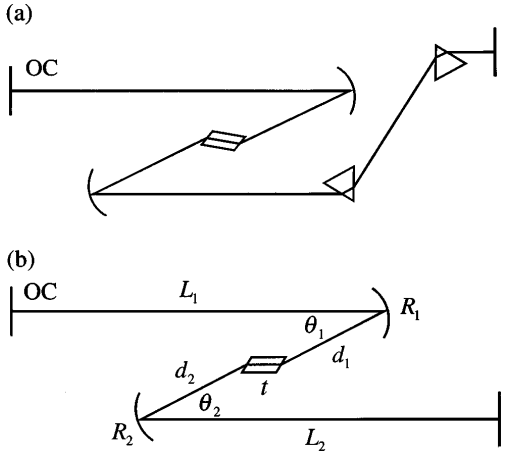

Fig. 5. (a) Z-shaped laser cavity of the sort used in a self-mode-locked Ti:sapphire laser. OC is the output coupler. (b) Equivalent cavity for quasi-cw conditions. For the example described in the text the distances are $L_1 = L_2 = 80$ cm, $d_1 = 4.85$ cm, $d_2 = 4.95$ cm, $t = 1.5$ cm, and $R_1 = R_2 = 10$ cm. The angles are $\theta_1 = \theta_2 = 27°$.

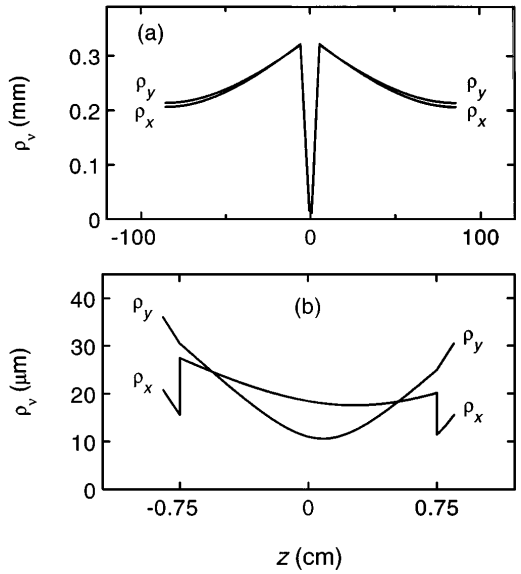

Fig. 6. Cavity solution for cw operation. The horizontal axis shows the position in the cavity, z, with zero at the center of the crystal and negative values on the side of the output coupler. The vertical axis shows rms widths ρ_x and ρ_y. (a) View of the entire cavity. (b) Magnified view of the crystal.

A. Mode-Locked Case: Nonlinear Coupling Neglected

If we neglect nonlinear coupling, then we can use an analytical procedure to find the cavity solutions. This analytical procedure can be applied to either the tangential or the sagittal plane, but, for this example, we consider the sagittal plane. We begin by labeling three points in the cavity for future reference. Points 1, 2, and 3 refer to the beam waists at the positions inside the crystal, at the output coupler, and at the other end mirror, respectively. We first propagate from point 1 to point 2. Inasmuch as $R_{y1} = R_{y2} = \infty$, the reduced q parameters are, from Eq. (3),

$$q_{\nu 1} = -i4\pi\rho_{\nu 1}^2/\lambda_0, \qquad q_{\nu 2} = -i4\pi\rho_{\nu 2}^2/\lambda_0 . \tag{10}$$

We next construct the *ABCD* matrix from point 1 to point 2. To do this we use standard linear *ABCD* matrices for the cavity elements and propagation distances, along with the *ABCD* matrix for nonlinear propagation within the crystal. Under the conditions considered here the latter *ABCD* matrix is[5]

$$M_y = \sqrt{1-\gamma_y}\begin{bmatrix} 1 & h/n_0 \\ -n_0\gamma_y/h(1-\gamma_y) & 1 \end{bmatrix}, \tag{11a}$$

where

$$\gamma_y = \frac{P}{P_c}\left[1 + \left(\frac{4\pi n_0 \rho_{1y}^2}{h\lambda_0}\right)^2\right]^{-1} \tag{11b}$$

and h is the propagation distance within the nonlinear medium. To obtain Eqs. (11), substitute Eq. (3), with $R_1 = \infty$, into the transformation rule for real *ABCD* matrix elements,[11]

$$q_{y2} = \frac{\tilde{A}_y q_{y1} + \tilde{B}_y}{\tilde{C}_y q_{y1} + \tilde{D}_y}, \tag{12}$$

separate the real and imaginary parts, and compare the result with Eqs. (I.30).

We let $\tilde{A}_y$, $\tilde{B}_y$, $\tilde{C}_y$, and $\tilde{D}_y$ be the matrix elements for propagation from point 1 to point 2. We substitute these matrix elements, along with the reduced q parameters of Eqs. (10), into Eq. (12), then separate the real and the imaginary parts to solve for the size of the beam waist in the crystal.

We repeat the above procedure for propagation from point 1 to point 3. For a self-consistent cavity solution, both calculations must give the same value for the size of the beam waist in the crystal. We obtain the two curves of Fig. 7 by plotting the results of the calculations for the propagation paths from point 1 to point 2 and from point 1 to point 3 under the condition that $P = P_c/2$. The horizontal axis of Fig. 7 gives the position of the beam waist z_c relative to the crystal center, and the vertical axis gives the width of the beam waist in the crystal, ρ_{yc}. The cavity solutions correspond to the intersections of the two curves, which occur in three places. We check whether these solutions are stable against perturbation[21] by using a method that we will describe presently. We find that the solutions corresponding to positions A and B of Fig. 7 are stable against perturbation. The solution corresponding to position C, however, is not stable against perturbation and therefore cannot be maintained within the cavity. The cavity solutions corresponding to points A and B are shown in Figs. 8(a) and 8(b), respectively. Figures 9(a) and 9(b) show the corresponding magnified views in the vicinity of the crystal. In a previous paper[6] we considered the same cavity discussed in this section, but in that paper we did not notice the existence of the second stable cavity solution.

Perhaps the most striking feature of the above result is that there are two stable cavity solutions. Such a result is not possible in a linear cavity, which can have at most one fundamental solution for a single cavity configuration.[19] The fact that nonlinear cavities can have multiple solutions if nonlinear coupling is neglected was pointed out previously.[5] It was also shown previously that a nonlinear cavity can have multiple solutions if nonlinear coupling is included.[6]

B. Mode-Locked Case: Nonlinear Coupling Included

We have just seen that one can use analytical techniques to find the cavity solutions of a self-mode-locked laser if nonlinear coupling is neglected. If nonlinear coupling is included, however, there are no analytical techniques

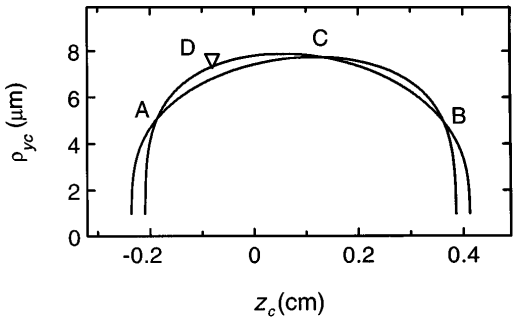

Fig. 7. Graphical solutions for the size of the beam waist, ρ_{yc}, inside the crystal versus the position of the beam waist with respect to the crystal center, z_c. Points A–C are the solutions obtained when nonlinear coupling is neglected. Points A and B are stable against perturbation; point C is not. Point D is the solution obtained when nonlinear coupling is included.

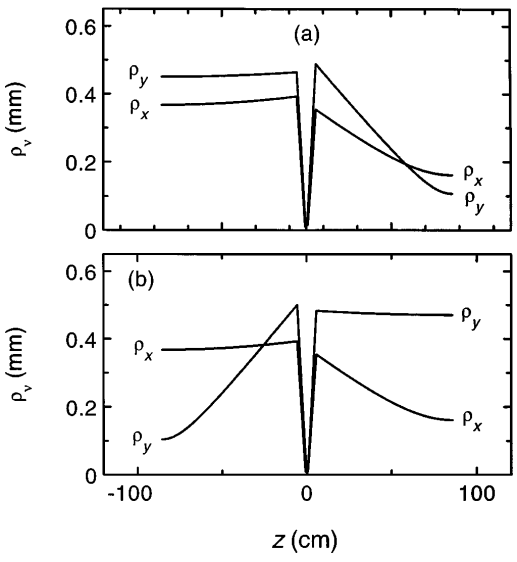

Fig. 8. Cavity solutions obtained when nonlinear coupling is neglected. (a) Solution corresponding to point A of Fig. 7. (b) Solution corresponding to point B of Fig. 7.

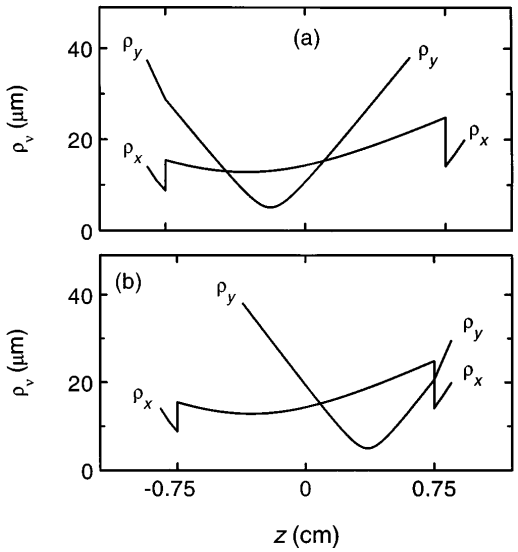

Fig. 9. Magnified views of the solutions shown in Fig. 8 in the vicinity of the crystal. (a) Solution corresponding to point A of Fig. 7. (b) Solution corresponding to point B of Fig. 7.

available for finding the cavity solutions. Instead, we have to bounce the beam back and forth in the cavity until a solution is obtained. In the case of a cavity that includes transverse variations in loss and gain, this procedure alone may be enough to yield the cavity solutions. It is not enough in the example considered here, however, as gain and loss have been neglected. In this case, at a position z' in the cavity, the beam widths $\rho_x(z')$ and $\rho_y(z')$ oscillate back and forth about some central values (without converging) on successive round trips. In effect, the cavity behaves like an undamped harmonic oscillator.

To get around this problem we introduce damping into the cavity. We use the term damping not because loss is introduced, but because the effect of the technique is to cause a gradual reduction in the size of the oscillations about the central value, so that the oscillations have the appearance of being damped. To understand the damping technique we recall from our previous discussion that, in a standing-wave cavity without gain, the beam is at a waist at the flat end mirrors. This means that the radii of curvature are infinite ($R_x = R_y = \infty$) and the chirp parameters are zero ($C_x = C_y = 0$) at these points. Initially, the beam widths ρ_x and ρ_y are not known at the end mirrors, and we must guess at their values. Because there is some error in our guesses, a beam that begins with infinite radii of curvature ($R_\nu = \infty$) returns after a round trip with finite radii of curvature ($R_\nu \neq \infty$). To introduce damping into the cavity we simply adjust the radii of curvature (or chirp parameters) after each round trip to equal the correct values more nearly. The effect of this is to cause the oscillations to decrease on successive round trips. We can describe this procedure quantitatively by defining a damping factor δ that transforms the parameters at one of the end mirrors by the operation $1/R_\nu \rightarrow (1 - \delta)/R_\nu$ or, equivalently, $C_\nu \rightarrow C_\nu(1 - \delta)$. We see that $\delta = 0$ and $\delta = 1$ correspond to undamped and totally damped oscillation, respectively.

After we have found the cavity solutions, we must check each solution for stability against perturbation.[21] We do this by removing the damping (setting $\delta = 0$) and then selecting initial values for ρ_x and ρ_y that are close to, but not exactly at, the solution values. If, during successive round trips, the oscillations in ρ_x and ρ_y remain bounded within a nonexpanding envelope, the solution is stable against perturbation. Otherwise the solution is unstable against perturbation and cannot be maintained within the cavity.

Using the technique described above, we have calculated the solutions of the cavity of Fig. 5(b) while taking into account the effects of nonlinear coupling. The results are shown in Fig. 10. The dashed curves of this figure are obtained with the SME's, and the solid curves are obtained with the BPM with 1D FFT's. The solid and the dashed curves are barely distinguishable. The most important thing to notice in this result is that there is only one cavity solution when nonlinear coupling is taken into account, in contrast to the two cavity solutions of Figs. 8 and 9 obtained when nonlinear coupling is neglected. The size and location of the beam waist [in the sagittal (y) plane] inside the crystal can be determined from Fig. 10(b) and are marked in Fig. 7 as point D.

The BPM that we used to obtain Fig. 10 also yields information about the profile of the beam at all points in the cavity. The solid curves of Figs. 11(a) and 11(b) show the profiles of the beam at the output coupler in the x and the y directions, respectively. These profiles are indicated by the intensity ratios, $|u_x(x)|^2/|u_x(0)|^2$ and $|u_y(y)|^2/|u_y(0)|^2$. The dashed curve in each figure is the best-fit Gaussian profile. In this case the profiles in the x and y directions are flattened and peaked, respectively, in the center of the beam relative to the profile of a Gaussian.

The results shown in Figs. 8–10 demonstrate that it is important to include nonlinear coupling in cavity calculations. Depending on the method of calculation, for example, we would reach different conclusions about where a slit should be placed to encourage self-mode locking. From Figs. 6 and 10 we see that the correct location for a slit oriented in the x direction [to block the beam in the y

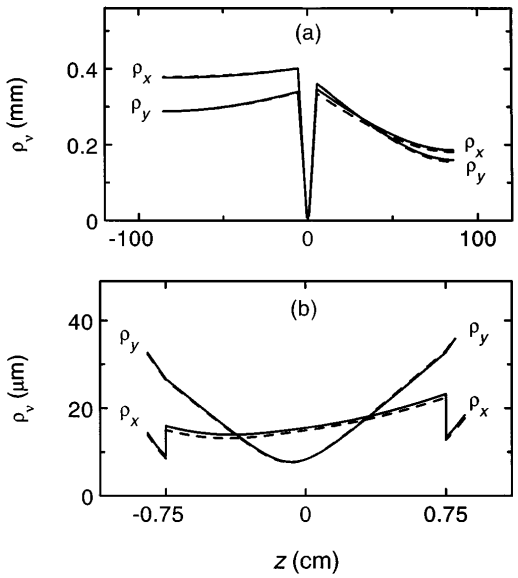

Fig. 10. Cavity solution, corresponding to point D of Fig. 7, that is obtained when nonlinear coupling is taken into account. The dashed curves show the solution obtained with SME's. The solid curves show the solutions obtained with the BPM with 1D FFT's. (a) View of the entire cavity. (b) Magnified view of the crystal.

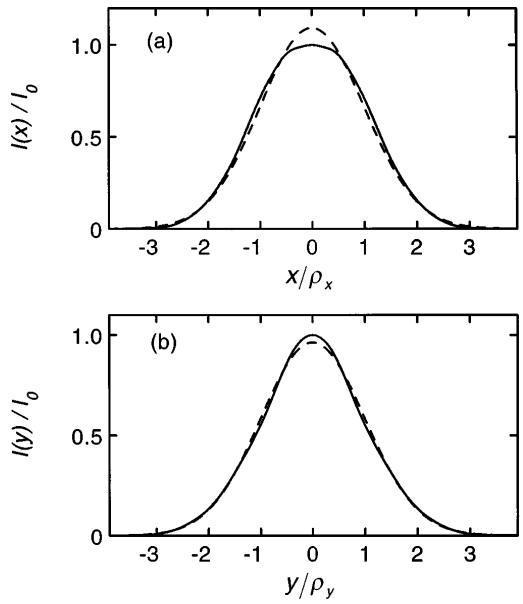

Fig. 11. Beam profile at the output coupler. (a) The horizontal axis gives the transverse position x/ρ_x, and the vertical axis gives the normalized intensity $I(x)/I_0$. The solid curve is the calculated profile, and the dashed curve is a Gaussian with the same rms width. (b) Same as (a), except for y instead of x.

(sagittal) direction] is on the prism (right) side. If nonlinear coupling were neglected, however, then from Figs. 6, 8, and 9 the location calculated for the slit could be either the left or the right side, depending on whether Fig. 8 or Fig. 9 were the dominant cavity solution. Note that these conclusions would be exactly reversed if the 4.85- and the 4.95-cm distances of Fig. 5(b) were switched.

Although we have used as an example the specific laser of Fig. 5(b), our modeling indicates that nonlinear coupling effects are important for a wide variety of cavity configurations. The cavity of Fig. 5(b) is near the center of a stability region, but dramatic effects that are due to nonlinear coupling can also be observed near the edges of the stability regions.[6]

It is important to recognize that the above analysis is incomplete because it does not include all the important physical effects. We have found that, for both cw and self-mode-locked lasers, there are usually quantitative differences in the results that we measure in the laboratory and the results that we calculate in the absence of thermal lensing and saturated gain. For example, if a cw laser is adjusted to the center of a stability region, the calculated and the measured distances are usually found to differ somewhat. Often, however, the calculated results are qualitatively correct, even if thermal lensing and saturated gain are neglected. The exception occurs when mode locking is brought about by a soft aperture, which cannot be treated without considering saturated gain. The computational techniques of Paper I can be extended to treat thermal and gain effects, but that is beyond the scope of this paper.

The cavity techniques that are developed here can be extended to treat the three-dimensional (x, y, t) case in which dispersive effects are important. This is done by use of techniques similar to those of Section 3. Such a treatment makes possible the determination of pulse width throughout the cavity.

6. SUMMARY

In the preceding paper we introduced two new computational techniques that take into account the effects of nonlinear coupling on the evolution of a beam propagating in a nonlinear, dispersive medium. These two new techniques involved (1) coupled second-moment equations and (2) the beam-propagation method with 1D FFT's to solve coupled differential equations.

In this paper we applied these computational techniques to the analysis of a self-mode-locked laser. We approached the problem in stages. We began with the propagation of a beam in a nonlinear medium for the quasi-cw case in which pulse width does not change significantly during propagation. We next looked at the short-pulse case in which dispersive effects need to be considered. We then discussed general techniques for including optical elements such as mirrors, angled interfaces, and prisms. Finally, we considered cavity effects.

We found that the accuracy of the calculations depended on the computational method used. For both the quasi-cw and the short-pulse cases we found that, with nonlinear coupling included, the methods gave relatively small errors. With nonlinear coupling neglected, however, we found the errors to be much larger.

We investigated the sources of error in the computational techniques of Paper I (with nonlinear coupling included). We found the main source of error in the calculations using the second-moment equations to be the result of (unaccounted for) changes in the shape factors (beam-quality factors and nonlinear shape factors). We found that the main source of error in the beam-propagation method using 1D FFT's to be the result of the electric-field amplitude's becoming nonseparable in rectangular coordinates. The latter error, however, was found to be very small.

We found that the effects of nonlinear coupling are often made more dramatic by the presence of a cavity. Using a specific example of a self-mode-locked Ti:sapphire laser, and neglecting nonlinear coupling, we found two fundamental cavity solutions that were stable against perturbation. With nonlinear coupling included, however, we found there to be only one fundamental cavity solution. Our modeling has indicated that nonlinear coupling is important in a wide variety of cavity configurations. We have observed, in the calculated results, dramatic effects that are due to nonlinear coupling in cavities operating near the edges, as well as near the centers, of the stability regions.

We showed how to carry out an analytical procedure to find the cavity solutions for the case in which nonlinear coupling is neglected. When nonlinear coupling is included, however, analytical techniques are not available. To get around this problem we introduced a damping technique that causes the beam to converge to the cavity solution as it is bounced back and forth in the cavity.

The cavity calculations in this paper have been carried out for the quasi-cw case in which the pulse width is relatively long (say, 100 fs). The techniques developed here, however, can be extended to the short-pulse case by inclusion of second-order dispersion (and higher-order dispersive effects if necessary). Such a treatment permits the determination of pulse width throughout the cavity.

This paper has demonstrated the importance of nonlinear coupling in calculations on self-mode-locked lasers. We have concentrated on the effects of diffraction, second-order dispersion, and Kerr nonlinearity, but a complete analysis of a self-mode-locked laser should account for other important effects such as thermal lensing and saturated gain. The techniques developed in this paper and in Paper I are very general and can be extended to include such effects. Although this paper has concentrated on the self-mode-locked laser, nonlinear coupling may be important in any physical system in which an intensity-dependent nonlinearity, such as Kerr nonlinearity, thermal nonlinearity, or saturated gain, is present.

APPENDIX A: COMPUTATION TIME

Whether the calculations are carried out with the SME's or the BPM, the time needed for performing a cavity calculation is affected by the number of steps required within the nonlinear medium. We can show, for the case of two dimensions (x and y), that the fractional error in the x dimension associated with a particular step size h is, in many cases, given approximately by[22]

$$|\text{error}| \approx \left(h/\rho_x^2\right)^2 |f(x, C_x, C_y, \epsilon_x^{(2)})|, \tag{A1}$$

where f is a function of the transverse position (x), the chirp parameters (C_x and C_y), and the ellipticity ($\epsilon_x^{(2)}$). To keep the relative error at an acceptable level, it is necessary to maintain h/ρ_x^2 at some small value; in other words, the step size h must be reduced as ρ_x decreases. If a cavity is adjusted to approach the edge of a stability region, then ρ_x or ρ_y approaches zero at the beam waist in the crystal. Consequently the step size approaches zero, and the computation time approaches infinity.

If the calculations are carried out with the BPM, then the time needed for performing a cavity calculation is also affected by the rms space–time-bandwidth product P_ν, defined for the 1D case as

$$P_\nu = \rho_\nu \Delta_\nu . \tag{A2}$$

Here ρ_ν is the rms width in the dimension $\nu = x$, y or t, and Δ_ν is the rms width in k_ν (the frequency space of ν). We assume that the beam profile in the ν dimension is relatively smooth and simple. We also assume that the FFT scaling is kept adjusted so that the widths ρ_ν and Δ_ν occupy approximately the same number of FFT points. It then can be shown that the number of points N_ν required for an FFT calculation is approximately proportional to the rms space–time-bandwidth product; that is, $N_\nu \propto P_\nu$. The overall computation time is determined by the number of individual calculations, which for a 1D FFT is of the order of $N_\nu \log_2 N_\nu$.[23]

To get a rough estimate of P_ν we consider the case in which the nonlinear effects are negligible, and we suppose that the profile is Gaussian. Then, from Eq. (I.30a), we obtain

$$\rho_\nu = \rho_{\nu 0}\sqrt{1 + \left(h/z_{d\nu 0}\right)^2}, \tag{A3}$$

where $\rho_{\nu 0}$ is the rms width at the beam waist, h is the distance of propagation from the beam waist, $z_{d\nu 0} = d_\nu/2\rho_{\nu 0}^2$ is the Rayleigh range, and d_ν is the dispersion-diffraction distance, defined in Eq. (I.21). It is well known that $\Delta_{\nu 0} = 1/2\rho_{\nu 0}$ for an unchirped Gaussian function.[24] Substituting this result and Eq. (A3) into Eq. (A2), we obtain

$$P_\nu = 1/2\sqrt{1 + \left(h/z_{d\nu 0}\right)^2}. \tag{A4}$$

If we propagate far away from the beam waist, then $P_\nu = h/2z_{d\nu 0}$. In the cavity of Fig. 5(b) we see that the largest number of points N_ν will be required near the folding mirrors, far away from the beam waist in the crystal. At these positions it may be necessary to set N_ν to several thousand to get accurate results. In the segments between the folding mirrors and the end mirrors, however, the number of points required is reduced because the relevant Rayleigh range is that corresponding to the beam waists of the end mirrors, not of the crystal. One way to reduce computation time is to write an autoranging routine to increase or decrease the number of transverse points as needed during propagation.

The number of points required for carrying out the BPM with 2D FFT's is approximately $N_x N_y \propto P_x P_y$, and the corresponding number of individual calculations is of the order of $N_x N_y \log_2(N_x + N_y)$.[23] Similarly, the number of points required for carrying out the BPM with 3D FFT's is approximately $N_x N_y N_t \propto P_x P_y P_t$, and the corresponding number of individual calculations is of the order of $N_x N_y N_t \log_2(N_x + N_y + N_t)$. Clearly, there is a huge increase in the required computation time in moving from 1D FFT's to 2D and 3D FFT's.

ACKNOWLEDGMENTS

This research was supported by the U.S. Army Research Office through a University Research Initiative Center and by IMRA America.

*Present address, SpatialMetriX Corporation, 222 Gale Lane, Kennett Square, Pennsylvania 19348.

REFERENCES AND NOTES

1. Equations that begin with the Roman numeral I are from the preceding paper [Paper I: R. E. Bridges, R. W. Boyd, and G. P. Agrawal, "Multidimensional coupling owing to optical nonlinearities. I. General fomulation," J. Opt. Soc. Am. B **13,** 553–559 (1996)].
2. A. E. Siegman, *Lasers* (University Science Books, Mill Valley, Calif., 1986), Chap. 16.
3. I. H. Malitson, "Refraction and dispersion of synthetic sapphire," J. Opt. Soc. Am. **52,** 1377–1379 (1962).
4. This result can be obtained by Fourier-transform techniques or (approximately) by use of Eq. (3. 3.11) of G. P. Agrawal, *Nonlinear Fiber Optics,* 2nd ed. (Academic, Boston, 1995). The values $\beta_2 = 580$ fs^2/cm and $\beta_3 = 420$ fs^3/cm used in these calculations are found by use of the Sellmeier equation of Ref. 3.
5. V. Magni, G. Cerullo, and S. De Silvestri, "*ABCD* matrix analysis of propagation of Gaussian beams through Kerr media," Opt. Commun. **96,** 348–355 (1993).
6. R. E. Bridges, R. W. Boyd, and G. P. Agrawal, "Effect of beam ellipticity on self-mode locking in lasers," Opt. Lett. **18,** 2026–2028 (1993).
7. Ref. 2, Chap. 15.
8. M. Born and E. Wolf, *Principles of Optics* (Pergamon, Oxford, 1987), Chap. 5.

9. A. E. Siegman, "Analysis of laser beam quality degradation caused by quartic phase aberrations," Appl. Opt. **32,** 5893–5901 (1993).
10. M. H. Dunn and A. I. Ferguson, "Coma compensation in off-axis laser resonators," Opt. Commun. **20,** 214–219 (1977).
11. Ref. 2, Chap. 20.
12. B. E. Lemoff and C. P. J. Barty, "Cubic-phase-free dispersion compensation in solid-state ultrashort-pulse lasers," Opt. Lett. **18,** 57–59 (1993).
13. R. L. Fork, O. E. Martinez, and J. P. Gordon, "Negative dispersion using pairs of prisms," Opt. Lett. **9,** 150–152 (1984).
14. I. P. Christov, M. M. Murnane, H. C. Kapteyn, J. Zhou, and C.-P. Huang, "Fourth-order dispersion-limited solitary pulses," Opt. Lett. **19,** 1465–1467 (1994).
15. Ref. 2, Chap. 18.
16. M. Lax, G. P. Agrawal, M. Belic, B. J. Coffey, and W. H. Louisell, "Electromagnetic-field distribution in loaded unstable resonators," J. Opt. Soc. Am. A **5,** 731–742 (1985).
17. O. Haderka, "Influence of diffraction on hard-aperture Kerr-lens mode locking," Opt. Lett **20,** 240–242 (1995).
18. A. Agnesi, G. C. Reali, "Analysis of unidirectional operation of Kerr lens mode-locked ring oscillators," Opt. Commun. **110,** 109–114 (1994).
19. Ref. 2, Chap. 21.
20. F. Salin and J. Squier, "Gain guiding in solid-state lasers," Opt. Lett. **17,** 1352–1354 (1992).
21. L. W. Casperson, "Mode stability of lasers and periodic optical systems," IEEE J. Quantum Electron. **QE-10,** 576–586 (1983).
22. M. Lax, J. H. Batteh, and G. P. Agrawal, "Channeling of intense electromagnetic beams," J. Appl. Phys. **52,** 109–125 (1981), Eq. (B20).
23. W. H. Press, S. A. Teukolsky, W. T. Vetterling, and B. P. Flannery, *Numerical Recipes in FORTRAN* (Cambridge U. Press, Cambridge, 1992), Chap. 12.
24. R. N. Bracewell, *The Fourier Transform and Its Applications* (McGraw-Hill, Singapore, 1986), Chap. 8.